Text S1.

In the model, energy and water exchanges between land and the atmosphere, and the soil water budgets are simulated at a 30 min time step. The parameterization of soil water dynamics is from De Rosnay et al. (2000, 2002). Vertical diffusion of water in the 11 soil layers (with a total depth of 2.0 m) of the soil column is solved by the Fokker-Planck equation, with hydraulic conductivity and diffusivity defined by the Mualem - Van Genuchten model (Van Genuchten, 1980; Mualem, 1976). Processes related to the carbon cycle such as plant phenology, photosynthates allocation, litter and soil C decomposition are calculated at a daily time step (Krinner et al., 2005).

A new plant functional type (PFT) with shallow roots was introduced for peatland vegetation (Largeron et al., 2018). In grid-based simulations, peatland is a sub-grid hydrological soil unit (HSU) that receives surface runoff from surrounding non-peatland HSU in the same grid cell, and has its bottom drainage flux reduced to zero, thus a high water content can be maintained in the peatland HSU where the standing water above the soil surface can reach up to 10 cm (Largeron et al., 2018). Qiu et al. (2018) improved the representation of peatlands in a revision referred to as ORCHIDEE-PEAT by implementing peat-specific hydraulics in the peatland HSU with high water content at saturation and high saturated hydraulic conductivity, while hydraulic parameters of non-peatland HSUs are determined by the dominant soil texture in the grid cell.

Text S2.

Following the CENTURY model (Parton et al., 1988), prescribed fractions of plant residues are added to the metabolic and structural litter pools. Litter from leaf and fruit of peat PFT is added to the top layer of litter pools, while belowground litter from root is added in depth discretized according to the exponential root profile of the peat PFT. To account for the fact that peatland vegetation develops shallow and extensive root systems to survive in the high stress conditions (a scarcity of oxygen and nutrients; spongy, acid soil) (Boutin and Keddy, 1993), the exponential root profile of the peat PFT is set an e-folding length of 30cm (Largeron et al., 2018). The fraction of litter that

31 is not respired into CO_2 provides C input to the active, slow and passive soil C pools,

32 with different fractions prescribed according to litter type and its lignin content (Zhu et

33 al., 2016). Decomposition of litter is controlled by temperature and litter humidity (Text

34 S3). For permafrost regions, litter C below the modelled local active layer thickness

35 (ALT) are set to zero and adjusted above the ALT to conserve the total input mass.

36

37 **Text S3.**

38 **Temperature inhibition function:**

39
$$f_{T,l} = \begin{cases} Q_{10}^{\left(\frac{T_l - T_{ref}}{10}\right)}, & T_l \geq 0°C \\ (T_l + 1) \times Q_{10}^{\frac{(0 - T_{ref})}{10}} & -1°C < T_l < 0°C \\ 0, & T_l \leq -1°C \end{cases}, \text{ with } Q_{10} = 2 \text{ and } T_{ref} =$$

40 30°C ,   (1)

41 where T_l (°C) is the soil temperature at the layer l, Q_{10} is the proportional decrease

42 in decomposition rate for a 10 °C decrease in temperature.

43 **Moisture inhibition function:**

44 The volumetric water content ($m^3 m^{-3}$)-respiration relationship for organic soils (with

45 organic carbon content: 50 mg g^{-1}) is from Moyano et al. (2012). Firstly, soil respiration

46 is assumed to respond to a change in soil moisture proportionally to the value of

47 respiration itself, the Proportional Response of Soil Respiration (PR_{SR}) is predicted for

48 each 0.02 soil moisture interval using the empirical relationship between PR_{SR} and

49 soil moisture:

50 $PR_{SR,l} = 1.22 - 0.94\theta_l + 1.84\theta_l^2 - 1.56\theta_l^3$,   (2)

51 where $PR_{SR,l}$ is the proportional response of soil respiration related to a 0.02 increase

52 in soil moisture at layer l, θ_l ($m^3 m^{-3}$) is the volumetric water content of layer l. Then,

53 soil respiration (SR) is calculated for each 0.02 moisture interval as below (Eq.5 in

54 Moyano et al., 2012):

55 $$SR(\theta) = \left(\prod_{k=\theta_0}^{\theta} PR_{SR_k} \right) \cdot SR_0 ,$$ (3)

56 where $SR(\theta)$ is the soil respiration when the volumetric water content is θ, SR_0 is

57 the initial soil respiration value and is set to 1 arbitrarily, θ_0 is the initial volumetric

58   water content and is set to 0.01, k is the soil volumetric water content at 0.02 moisture

59   interval from the initial moisture (θ_0) to θ.

60   Finally, relative respiration is calculated by dividing SR value in each 0.02 moisture

61   interval by the maximum value obtained. The specific moisture modifier ($f_{M,l}$) value

62   was diagnosed at each time-step according to the simulated volumetric water content.

63

64   **Text S4.**

65   **The cost-efficient TOPMODEL**

66   In TOPMODEL, sub-grid-scale topography information and soil properties of a given

67   watershed / grid cell are used to redistribute the grid-cell mean water table depth to

68   delineate the extent of sub-grid area at maximum soil water content. This is achieved

69   by relating the local water table of a sub-grid pixel with the mean water table of a

70   watershed / grid cell, based on the spatial distribution of the compound topographic

71   index (CTI)

72   The CTI indicates the likelihood of a pixel to be inundated, a pixel with a larger CTI

73   having a greater potential to be inundated. With an assumed linear relationship between

74   the local water table depth and the grid mean water table depth (Eq. 4), the minimum

75   value of the topographic index (CTI*) for a pixel to get flooded (WT_i = 0) can be

76   calculated from Eq. 5.

77    $$WT_i - \overline{WT} = -\frac{1}{m}(CTI_i - \overline{CTI}) \ , \tag{4}$$

78    $$CTI^* = \overline{CTI} + m \cdot \overline{WT} \ , \tag{5}$$

79   where WT_i (in meters) is the local water table depth at pixel i, $\overline{WT}$ is the grid mean

80   water table depth, $\overline{CTI}$ is the mean CTI over the catchment, and m (m^{-1}) is the

81   saturated hydraulic conductivity decay factor with depth.

82   Accordingly, the flooded area of the grid cell consists of all its pixels with a local CTI

83   greater than CTI*, and therefore the flooded area fraction (f) can be calculated as the

84   ratio of the total area of flooded pixels (CTI > CTI*) and the total area of the grid cell.

85   To rule out pixels that have too low CTI values to be flooded (i.e. mountains, places

86   with steep slopes) even though the grid cell mean water table is quite shallow, CTI_{min}

87   is introduced to calculate the maximum possible flooded area fraction (f_{max}) of the grid

88 cell. Thus f_{max} is the ratio of the total area of pixels with CTI > CTI_{min} and the total

89 area of the grid cell. Lastly, the flooded area fraction of the grid cell can be calculated

90 as: $f_f = \min(f, f_{max})$.

91 An empirical relationship between f and $\overline{WT}$ can be established for a given grid cell

92 with a specific m value (Fig. S2a①), and this relationship can be approximated by an

93 asymmetric sigmoid function (Stocker et al., 2014):

94 $$f_{flood} = \left(1 + v \cdot e^{-k \, (\overline{WT_x} - q)}\right)^{-1/v} \, , \tag{6}$$

95 Finally, the flooded area fraction of the grid cell (f_f) can be replaced by $f_s =$

96 $\min(f_{flood}, f_{max})$ (Fig. S2a②).

97 As demonstrated by Stocker et al. (2014), the choice of m and CTI_{min} determines

98 the parameter set (v, k, q, f_{max}). In contrast to their study, in which m and CTI_{min} were

99 considered as tunable but globally uniform parameters, we tested different

100 combinations of m (m= (5,6,7,8,9,10,11,12,13,14,15)) and CTI_{min} ($CTI_{min} =$

101 (4,5,6,7,8,9,10,11,12)) at each grid cell and select the combination that matches with

102 the CW-WTD wetlands map (Tootchi et al., 2018).

103

104 **The water table position**

105 The grid mean water table depth is calculated as the area-weighted mean water table of

106 non-peatland soils (mineral soils) and peatland HSU:

107 $$\overline{WT} = WT_{peat} \cdot f_{peat} + WT_{mineral} \cdot f_{mineral} \, , \tag{7}$$

108 where WT_{peat} is the water table depth of the peatland HSU in the grid, f_{peat} the

109 peatland area fraction in the grid, $WT_{mineral}$ is the water table of mineral soils in the

110 grid, $f_{mineral}$ is the area fraction of mineral soils and equals to $1 - f_{peat}$.

111 Water table depth of mineral soils is calculated as the saturation deficit (in meters) in

112 the unfrozen part of the soil:

113 $$WT_{mineral} = \sum_{i=1}^{k} \left(\frac{\theta_i}{\theta s_{dominant}} \cdot \Delta Z_i\right) - \sum_{i=1}^{k} \Delta Z_i$$

114 $$\tag{8}$$

115 where θ_i is the soil water content (liquid and ice) of mineral soils HSU at the layer i,

116    $\theta s_{dominant}$ is the mineral soil water content at saturation and determined from the

117   dominant soil texture in the grid, ΔZ_i (m) is the thickness of the layer, i runs from the

118   top of the ground surface to the soil bottom, and k the uppermost non-frozen soil layer.

119   k is employed here to take into account the existence of frozen soil layers. However,

120   when the local non-frozen depth is low, water table level may be overestimated, causing

121   an overestimation of flooded area. Therefore, we set an arbitrary condition for the

122   calculation: the water table is calculated only when all soil layers in the top 18.6 cm (7

123   layers in total) are not frozen, otherwise, the water table is not calculated and the

124   flooded area fraction is zero.

125   The calculation of peatland water table includes standing water (WT_{ab}) of peatland

126   (Qiu et al., 2018) and includes a rough representation of the effect of free-phase gas

127   bubbles on water table level by subtracting a constant volumetric gas content (g_a) from

128   the saturated water content of peat (θs_{peat}):

129    $$WT_{peat} = WT_{ab} + \sum_{i=1}^{k}\left(\frac{\theta_i}{(\theta s_{peat} - g_a)} \cdot \Delta Z_i\right) - \sum_{i=1}^{k}\Delta Z_i$$

130   (9)

131   where WT_{ab} is the height of the above-surface water reservoir, θ_i is soil water

132   content of peat soil at the layer i, θs_{peat} is the peat soil water content at saturation, all

133   other parameters as defined in Eq. 8. The decomposition of peat produces several gases

134   (CH_4, CO_2, H_2S) and when the production of these gases exceeds their equilibrium

135   solubility in the soil solution, gas bubbles form (Kellner et al., 2005). As the bubbles

136   accumulate and/or grow, some of them get bigger than pore diameters and get trapped

137   in the peat matrix, which may further block the movement of water and gases, causing

138   development of closed zones or layers — the "bubbles confining layers" (Glaser et al.,

139   2004; Kellner et al., 2005; Romanowicz et al., 1995). Volumetric content of trapped gas

140   in peat was estimated to range from 0 to 0.2, whether a confining layer exists or not

141   (Comas et al., 2011; Donald O. Rosenberry et al., 2006; Strack et al., 2005). As noted

142   by several studies, entrapped gas bubbles affect both peatland hydrology and

143   biogeochemistry (Baird and Waldron, 2003; Donald O. Rosenberry et al., 2006; Strack

144   et al., 2005). Kellner et al. (2005) explicitly discussed how changes in gas bubble

145   volume in the saturated zone of peat can alter the water table level: increase of bubble

146   volume can push water out of pores in the saturated zone, resulting in a higher water

147   table by pushing water upward; at the same time, the peat surface can be raised if the

148   peat profile is compressible. The latter phenomena has been supported by observations

149   and experiments in peatlands (Glaser et al., 2004; Strack et al., 2006), while the former

150   is difficult to quantify in the field because the fluctuation of peat surface complicates

151   the situation. The model cannot simulate dynamics of entrapped gases now, thus we

152   subtract a constant gas fraction of 0.08 (g_a) from θs_{peat} to represent the maximum

153   water content of peat. This value has also been used by Wania et al. (2009a) in

154   calculation of the water table position in the LPJ-Why model. We acknowledge that our

155   representation of gas bubbles in the equation (Eq. 9) remains open to question,

156   considering that the accumulation of free-phase gases is temporally and spatially

157   variable, and the response of the water table level to the existence of gas bubbles might

158   be much more complicated than that represented by the equation.

159

160   **Text S5.**

161   According to the peatland distribution analysis by Gignac et al. (2000), $SWB = -6$ cm

162   is the minimum value at which the *Sphagnum*-dominated peatland can be found in

163   western Canada, and this threshold works well in predicting the geographical

164   distribution of *Sphagnum*-dominated peatland in North America. Alexandrov et al.

165   (2016) proved that an excess of summer precipitation ($P_w > 0.7$ PET+30 mm yr^{-1}) is

166   necessary to keep a positive water balance for peatland and thus is a key factor in

167   determining peatland extent in West Siberia since the Last Glacial Maximum.

168

169   **Text S6.**

170   The initiation and development of northern peatlands followed the retreat of the ice-

171   sheets (Gorham et al., 2007; MacDonald et al., 2006). To take into account the

172   deglaciation of North America that triggered peatland expansion after ice sheet

173   disappeared, in regional simulations, we define *N* and *X* according to the reconstructed

174   glacial retreat in North America by Dyke (2004) at discrete epochs (Fig. S5). We

assumed no peat inception before 12000 BP. At 12000 BP being the start of the Holocene (Fig. S5a), SubC was run for 12000 years ($X = 2$ ka, $N = 6$) for all un-glaciated areas (NA-120, Table S1). At 8900 BP (Fig. S5b), the Hudson Bay was still under the Laurentide Ice Sheet (Dyke, 2004). For areas that lost ice-sheet between 12000 BP and 8900 BP (NA-89, Table S1), the SubC was run for 5 times ($N = 5$), with the length of the last SubC being 0.9 ka ($X = 0.9$ ka). We used the latter date (8900 BP) to define values of N and X instead of using the middle date of the time interval, because newly deglaciated land was not immediately suitable for peat deposition and normally there was a lag between deglaciation and peatland initiation (Gorham et al., 2007; Harden et al., 1992; Payette, 1984). At 7400 BP (Fig. S5c), ice sheets nearly vanished and the Hudson Bay was ice-free while only the northern part of Quebec and the Baffin Island were still covered by ice. Thus we set $X = 1.4$ ka and $N = 4$ for all grid cells that lost ice-sheet between 8900 BP and 7400 BP (NA-74, Table S1). From 3200 BP (Fig. S5d), only a small last remnant of the Laurentide Ice Sheet only existed at Baffin Island, and we set $X = 1.2$ ka and $N=2$ for the newly exposed lands (NA-32, Table S1).

The Eurasian ice sheet complex reached its maximum area and volume at about 21−20 ka BP, however, from then on, the ice sheets retreated fast (Hughes et al., 2016). By 12000 BP only Norway, Sweden (except the southern tip), Finland, Svalbard islands, Franz Josef Land and northern Novaya Zemlya were covered by ice (Fig. S6a). The Scandinavian Ice Sheet was restricted to south of the main watershed in southeastern Norway and east of the watershed in Sweden by 10000 BP (Fig. S6b) and was postulated to have disappeared by 9000 BP or slightly earlier (Hughes et al., 2016). We divide Eurasia into two regions with different timings of deglaciation. First, for all un-glaciated areas by 12000 BP (Fig. S6a) we run the SubC for 6 times ($N = 6$) with $X = 2$ ka (EA120, Table S1). For glaciated areas at 12000 BP, we run the SubC for 5 times ($N = 5$) with $X = 0.9$ ka (EA89, Table S1).

Text S7.

Evaluation datasets for Northern peatlands area:

1. World Inventory of Soil Emission potentials (WISE):

The harmonized global soil profile dataset WISE comprises attribute data from 21000 soil profiles. Commonly used soil chemical and physical attributes are organic carbon, nitrogen (N), pH, cation exchange capacity of the soil, exchangeable nutrients, bulk density, weight percentages of sand, silt and clay-size materials etc. are considered in the dataset (Batjes, 2016). The database was compiled from the FAO Soil Database (FAO-SDB), various regional Soil and Terrain Databases (SOTER), the ISRIC-ISIS (Soil Information System), the Natural Resources Conservation Service (NRCS-USDA) and national contributions and soil surveys (Batjes, 2008, 2009). We queried the dataset for areas covered by histosols to approximate the distribution of peatlands and aggregated the data to the 1° grid of the model to compare with ORHCIDEE-PEAT v2.0 output.

2. Global peatland distribution map (PEATMAP):

Xu et al. (2018) developed an improved global peatland map (PEATMAP) by reviewing a wide variety of global, regional and local scale peatland distribution information. For areas of overlap between two or more datasets, the best source data are the ones that 1) are most likely to be directly relevant to peatland extents, 2) have the finest spatial resolution and 3) have been most recently updated. This PEATMAP product amalgamated the most detailed and up-to-date data sources on peatland distribution at fine spatial resolutions. The original PEATMAP dataset in shapefile format, with polygons holding information of coverage and area of individual peatlands and peat complexes was interpolated into a 1° grid.

3. International Mire Conservation Group Global Peatland Database (IMCG-GPD):

The IMCG-GPD database (Joosten, 2010) contains an inventory of peatlands for the years 1990 and 2008 at regional and national levels. The database integrates peatland proxies (vegetation, land use etc.), observations and reports. Extent and status of peatlands, volume of the peat resource and estimates of CO_2 emissions from different types of land use are included (Joosten, 2010).

We compare peat area estimates from these three datasets with the output of ORCHIDEE-PEAT v2.0 for the year 2008.

4. Peatland distribution map by Yu et al. (2010):

235 The qualitative peatland map of Yu et al. (2010) consists of irregular grids delineating
236 regions with the presence of peatlands (>5%) based on geological inventories of
237 countries/regions and histosols from the HWSD v1.1 (FAO et al., 2009). We projected
238 this binary data onto $0.05° \times 0.05°$ latitude-longitude grids and aggregated it on $1° \times 1°$
239 grids to obtain a map of peatlands fractional cover. This fractional cover map indicates
240 regions with significant peatland cover, not directly comparable to other quantitative
241 benchmark data. We use this map to visualize regions with significant cover of peatland
242 (Sect. 4.2).

243

244 **Soil organic carbon stocks:**
245 1. The WISE:
246 We queried the WISE database to extract bulk density and organic carbon content for
247 the histosols component for each soil mapping unit, and calculated the SOC density for
248 histosols after excluding the coarse soil fraction. Note that the WISE only has C
249 inventories to a depth of 2 m, while the model has a depth up to 48 m.
250 2. The IMCG-GPD:
251 We compared the carbon stocks estimate by IMCG-GPD in 2008 with the model output.
252
253
254
255
256
257
258
259
260
261
262
263
264

267 **Table S1.** Information for the peat cores included in the site simulation, and for the
268 regions included in the regional simulation. Peat cores are from the HPPB database
269 (Loisel et al., 2014). X: simulation years in the last SubC run, Y: number of years in the
270 transient simulation, N: number of acceleration procedures. For site simulation, $Y =$ the
271 year of coring – 1860, $X =$ the age of the core – $2000 \times (N–1) – 30 \times N – 100 – Y$; for
272 regional simulation, $Y = 150$, X is defined according to the pattern and timing of
273 deglaciation. NA-120, NA-89, NA-74, NA-32, EA-120 and EA-89 are derived from
274 reconstructed glacial retreat of North America and Eurasia, refer to Sect. 3.2, Fig. S5
275 and Fig.S6. Red lines are 15 sites for which peat age, depth, bulk density and fraction
276 of C are available so that observed C vertical profile can be built.

277

Site-level simulation								
Core name	Latitude	Longitude	Age	Coring year	Depth	X	N	Y
Hongyuan HYLK1	32.77	102.52	10827	2006	617.5	2431	5	146
Zoige	33.45	102.63	9996	2008	640.5	3628	4	148
Sidney bog	44.39	−69.79	10789	2010	724.0	2389	5	150
Covey Hill	45	−73.49	12720	—	309.0	2290	6	150
Petite Bog	45.14	−63.94	13474	2010	861.0	3044	6	150
Altay	48.12	88.35	11308	2010	729.5	2908	5	150
Lebel	49.1	−68.25	5831	2009	574.5	3522	2	149
Plaine	50.27	−63.54	7451	2009	356.5	3112	3	149
JBL8	50.47	−89.93	4481	2008	189.0	2173	2	148
JBL1	51.07	−89.8	6051	2008	285.0	1713	3	148
Burnt Village	51.13	−55.93	8526	2010	546.0	2156	4	150
KJ2-3	51.59	−81.76	4677	2009	245.5	2368	2	149
Mosaik	51.98	−75.4	7072	2006	296.5	2736	3	146
JBL2	52.02	−90.13	6742	2008	421.0	2404	3	148
Sterne	52.05	−75.17	7134	2006	286.0	2798	3	146
Goldeye Lake	52.46	−16.19	9207	1999	324.5	2848	4	139
Lac Le Caron	52.58	−75.83	7510	2006	481.5	3174	3	146
VC04-06	52.71	84.18	6599	2009	304.0	2260	3	149
JBL3	52.87	−89.93	7708	2008	244.5	3370	3	148
La Grande 3	53.57	−76.13	6816	2004	374.5	2482	3	144
Sundance Fen 03-3	53.58	−116.75	10914	2003	438.5	2521	5	143
Upper Pinto Fen	53.58	−118.02	7699	1999	385.0	3370	3	139
La Grande 2	53.65	−77.73	6543	2004	319.5	2209	3	144
KAM12-C4	54.01	156.08	12708	2012	395.5	2276	6	152
Ours 1	54.05	−72.45	5491	2005	109.5	3186	2	145
JBL7	54.4	−89.52	7607	2008	330.0	3269	3	148

HL-02	54.61	−84.6	4494	2011	229.5	2183	2	151
Slave Lake bog	55.06	−114.13	10285	1989	384.0	1906	5	129
KUJU-PD2	55.23	−77.7	5084	2008	243.5	2776	2	148
JBL4	55.27	−88.93	6051	2008	175.5	1713	3	148
Joey Lake 7	55.46	−98.16	8256	2001	228.5	1895	4	141
Utikuma	55.84	−115.09	5079	2004	370.5	2775	2	144
Patuanak	55.85	−107.68	9017	2001	310.0	2656	4	141
Mariana Lake 03-1	55.9	−112.09	7222	2003	471.5	2889	3	143
Mariana Lake 03-3	56.02	−111.93	5872	2003	384.5	3569	2	143
86-Kvartal (Zh0)	56.33	84.58	8651	—	725.0	2281	4	150
Vasyugan (V21)	56.83	78.42	9709	—	1095.0	3349	4	150
Usinsk Mire 1	57.42	65.67	11634	1996	395.0	3248	5	136
Glen Carron	57.53	−5.15	10334	1994	360.0	1950	5	134
SIB06	58.44	83.43	8680	2001	365.5	2319	4	141
Lake 785	59.11	−97.4	6833	2012	157.5	2491	3	152
Lake 396	59.58	−98.57	6077	2012	95.5	1735	3	152
Selwyn Lake 1	59.88	−104.2	6452	2002	195.5	2120	3	142
Horse Trail	60.42	−150.9	12695	2005	413.0	2270	6	145
Kenai Gasfield 07-2	60.45	−151.25	11448	2007	283.1	3051	5	147
Bear	60.53	−145.45	10357	2010	351.5	1957	5	150
Swanson	60.79	−150.83	14065	2004	245.0	1611	7	144
V34	61.47	79.46	8824	1999	277.5	2465	4	139
Martin River	61.8	−121.4	7552	—	243.9	3212	3	150
Siikaneva	61.84	24.17	9622	2012	551.0	3250	4	152
Petersville (09-MC)	62.42	−150.68	13881	2008	256.5	3453	6	148
D127	64.31	70.29	10034	1999	199.5	1645	5	139
Nuikluk 10-2	64.83	−163.45	9143	2010	188.5	2773	4	150
NW-BG-2	65.21	−127.01	10932	2008	128.0	2534	5	148
Saarisuo	65.65	27.32	9138	1990	510.0	2788	4	130
E-110	66.47	76.99	9496	2000	192.5	3136	4	140
Rogovaya River 3	67.25	62.07	10088	1995	167.5	1703	5	135
Lompolojänkkä	68	24.22	9969	2010	215.0	3599	4	150
IN-BG-1	68.32	−133.42	9121	2007	375.0	2754	4	147
Stordalen	68.35	19.05	4717	2003	100.0	2414	2	143
Regional simulation								
	NA-120, EA-120	12000				2000	6	150
	NA-89, EA-89	8900				900	5	150
	NA-74	7400				1400	4	150
	NA-32	3200				1200	2	150

278

279

280
281

282
283
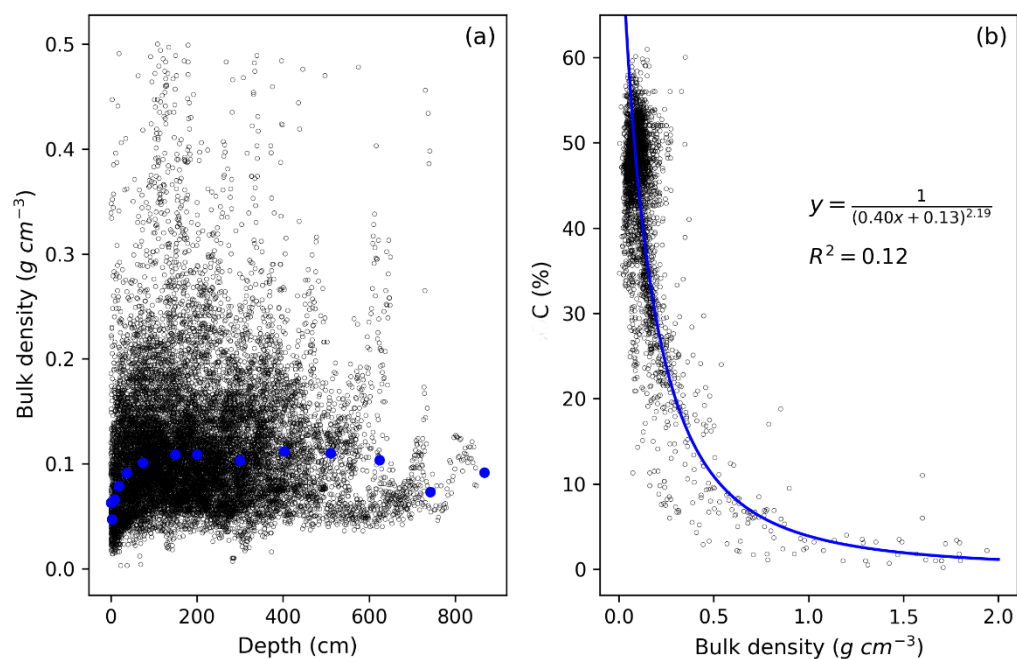
Fig. S1. (a) Measured bulk densities from 102 peat cores (black dots) and the median value at each depth bin (blue dots), (b) the relationship between soil carbon fraction (% weight) and bulk density.

287
288
289
290

291
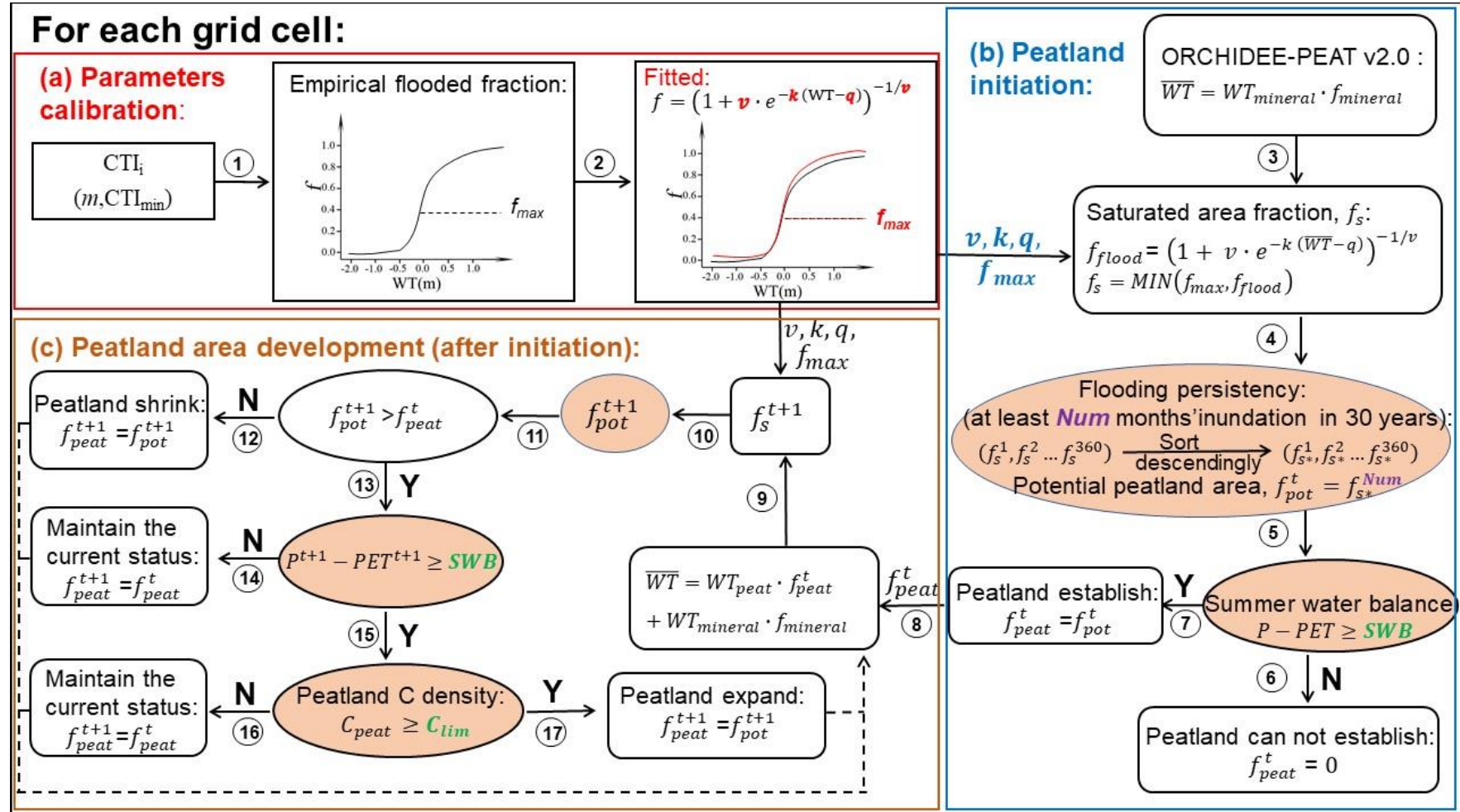
292 **Fig. S2.** Information flow of dynamic peatland area module in ORCHIDEE-PEAT v2.0. *Num* is a gridcell-specific parameter, *SWB* and C_{lim} are

293 globally uniform parameters (Sect. 2.2)
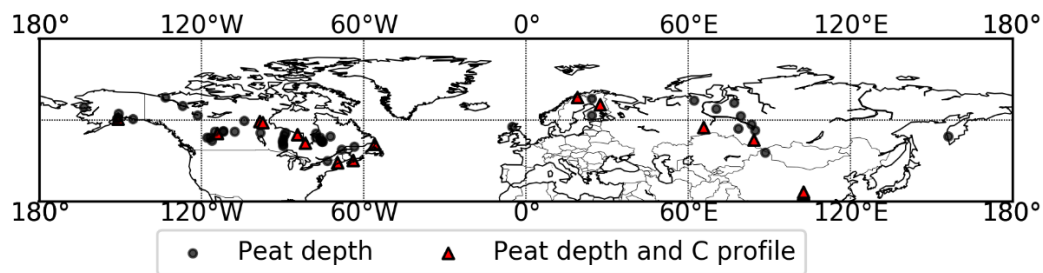
Fig. S3. Locations of the peatland cores used in site-level simulations. Marker: black circle – cores for which only peat age and depth were available, red triangle – cores for which peat age, depth, bulk density and carbon fraction were available so that C density vertical profile can be built.
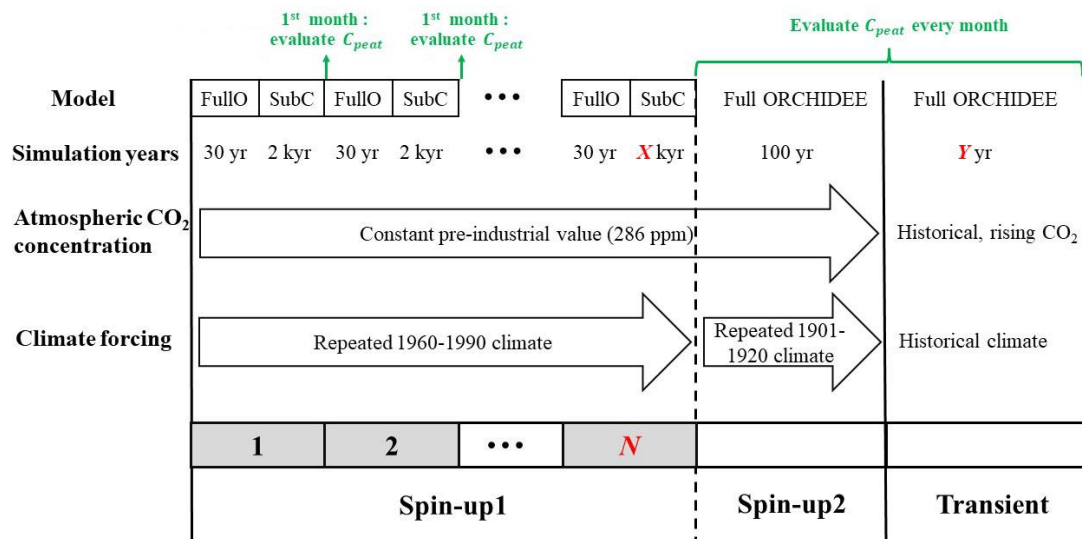
Fig. S4. Simulation Protocol. FullO: the full ORCHIDEE-PEAT v2.0 model, SubC: the soil carbon sub-model. Refer to Sect. 3.1 for detailed description of simulations.
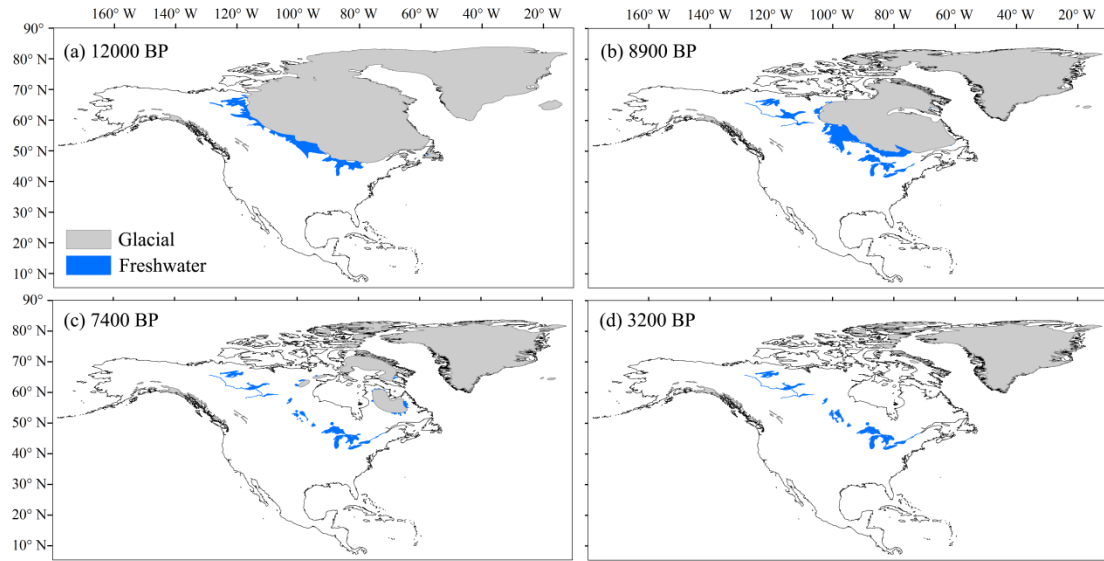
Fig. S5. Reconstructed maps of glaciated North America by (a) 12000 BP, (b) 8900 BP, (c) 7400 BP, (d) 3200 BP, redrawn from Dyke (2004).
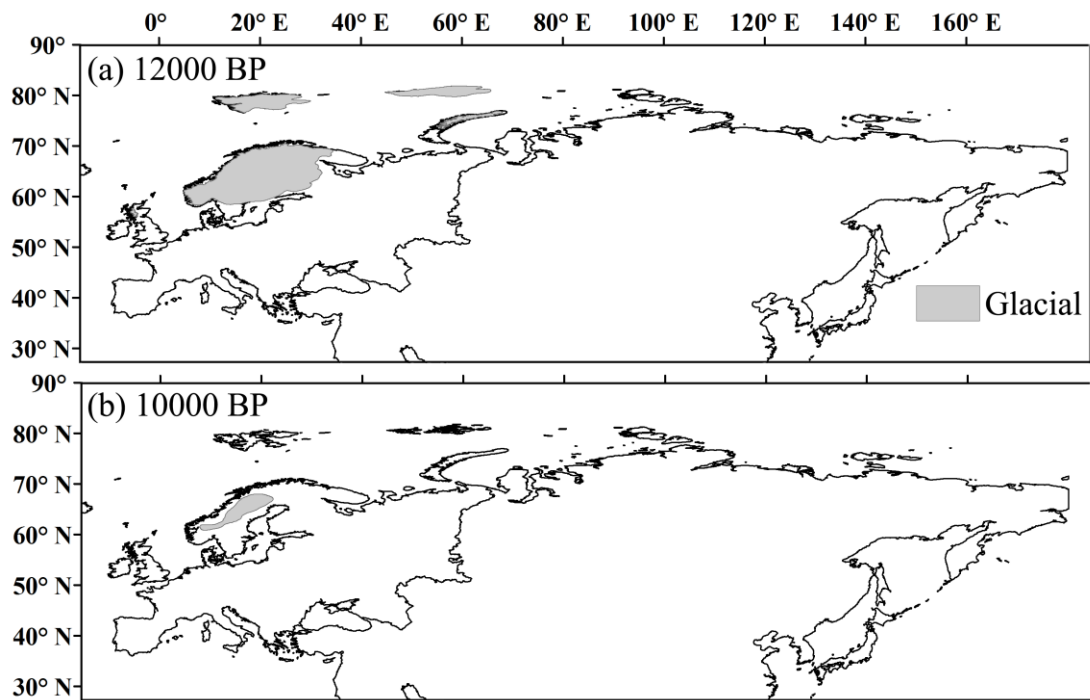
Fig. S6. Reconstructed glacial extent of Eurasia (>30° N) by (a) 12000 BP, (b) 10000 BP; redrawn from Hughes et al. (2016).
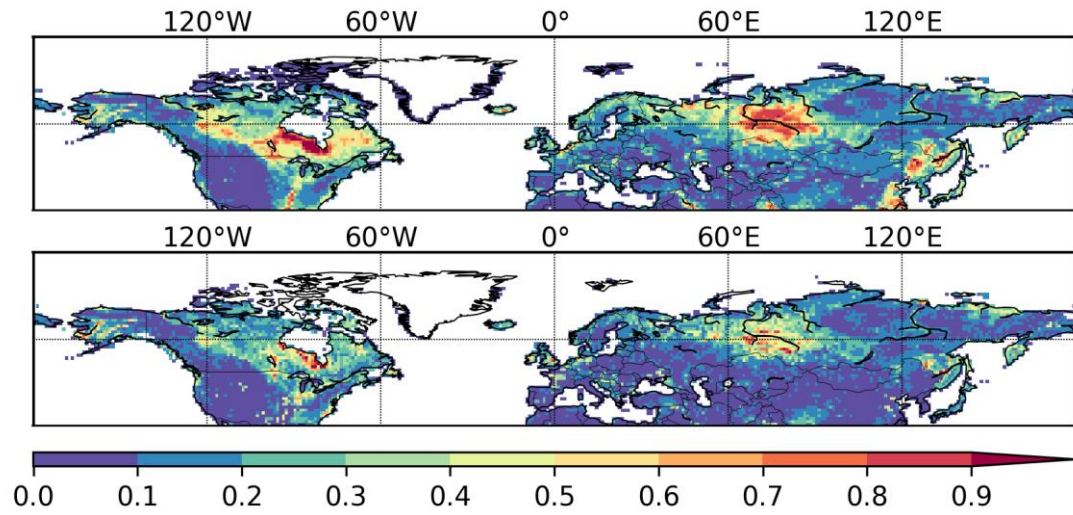
Fig. S7. Potential wetland areas from CW-WTD (upper panel), simulated maximum inundation areas (lower panel)
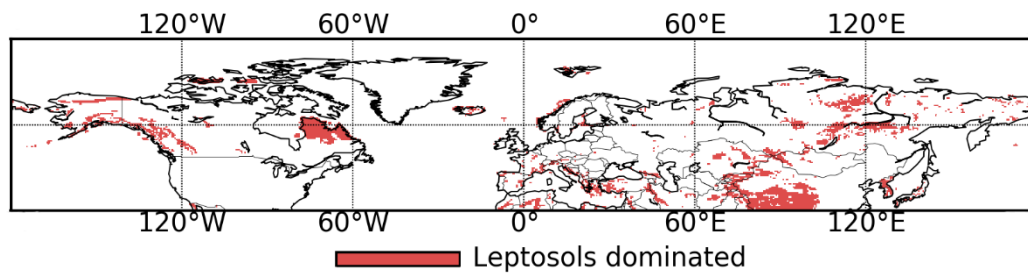
Fig. S8. Leptosols dominated grid cells, from the harmonized global soil profile dataset (WISE).
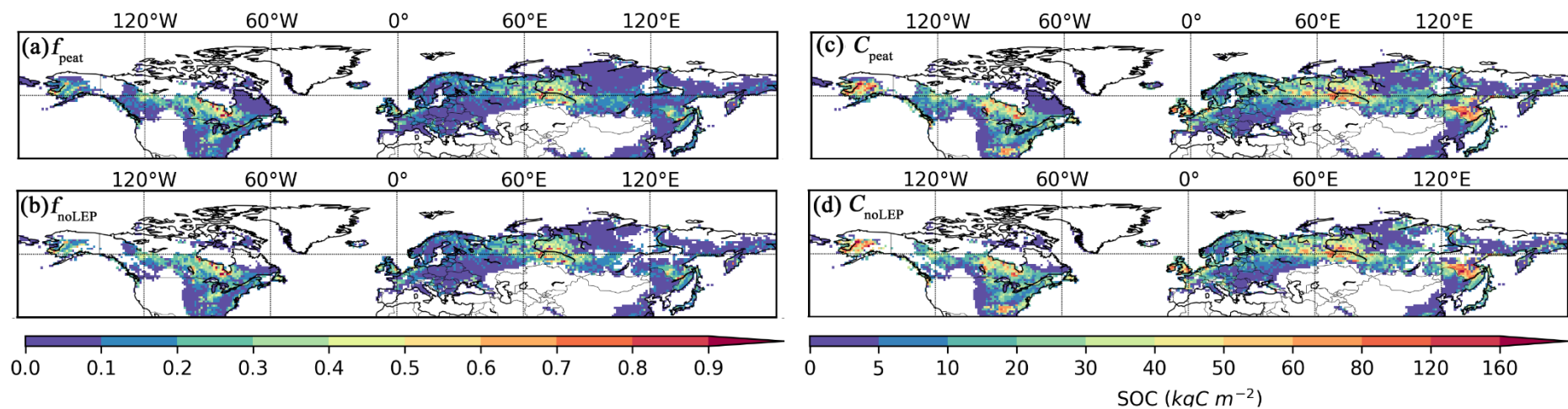
Fig. S9. (a) Simulated peatland area fraction (f_{peat}), with pattern and timing of deglaciation has been considered; (b) same as (a), but areas dominated by Leptosols have been masked; (c) simulated peatland soil carbon density (C_{peat}), with pattern and timing of deglaciation has been considered; (d) same as (c), but areas dominated by Leptosols have been masked.
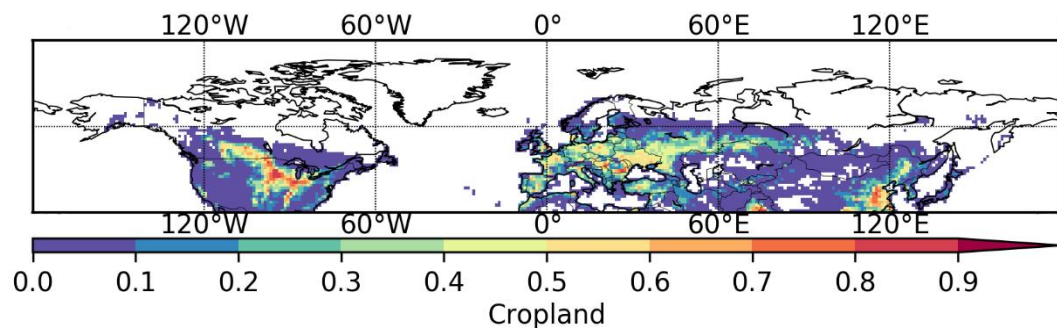
Fig. S10. Maximum monthly growing area fraction of 26 crops, from the global data set of monthly irrigated and rainfed crop areas around the year 2000 (MIRCA2000).
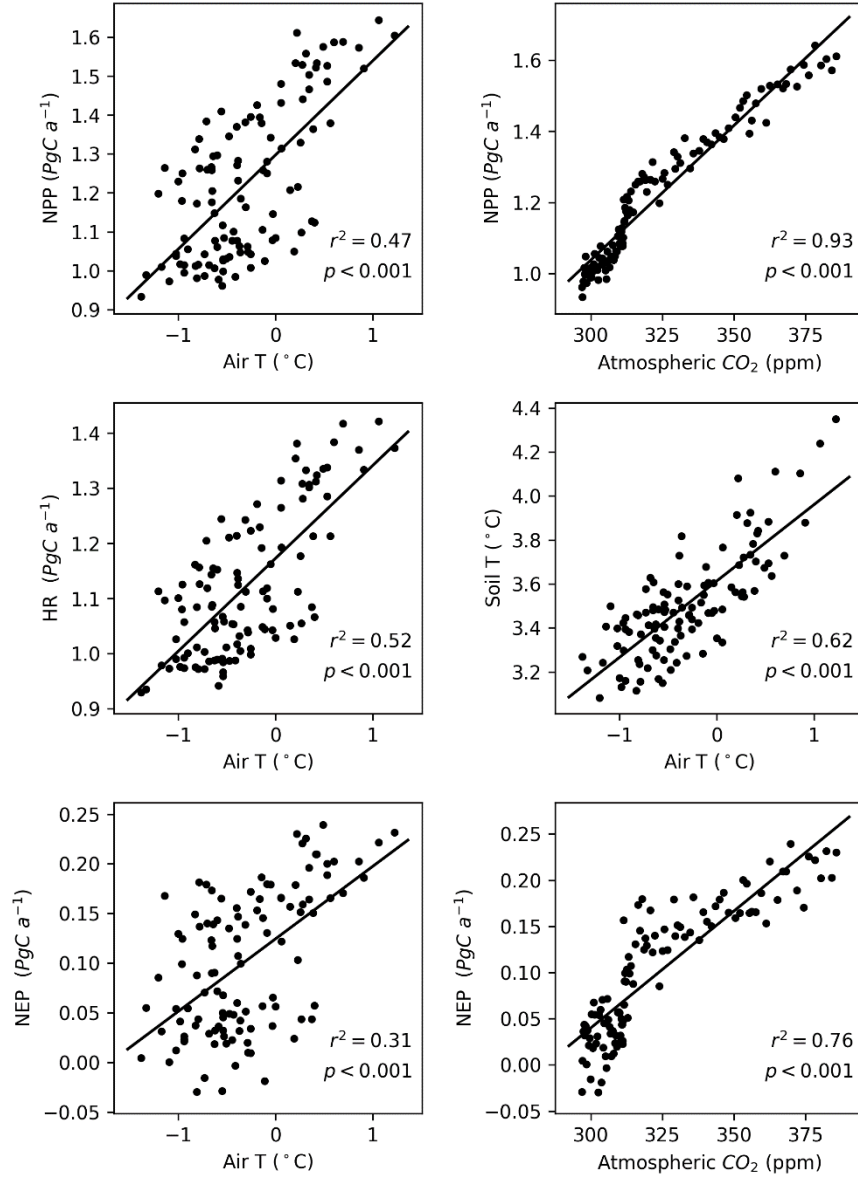
Fig. S11. Regression analysis for the relationship between (top-left) simulated net primary production (NPP) of northern peatlands and mean air temperature (T) of grid cells that have peatland, (top-right) NPP and atmospheric CO_2 concentration, (middle-left) heterotrophic respiration (HR) of northern peatlands and air T, (middle-right) simulated soil temperature at 25 cm and air T, (bottom-left) net ecosystem production (NEP) and air T, (bottom-right) NEP and atmospheric CO_2 concentration.
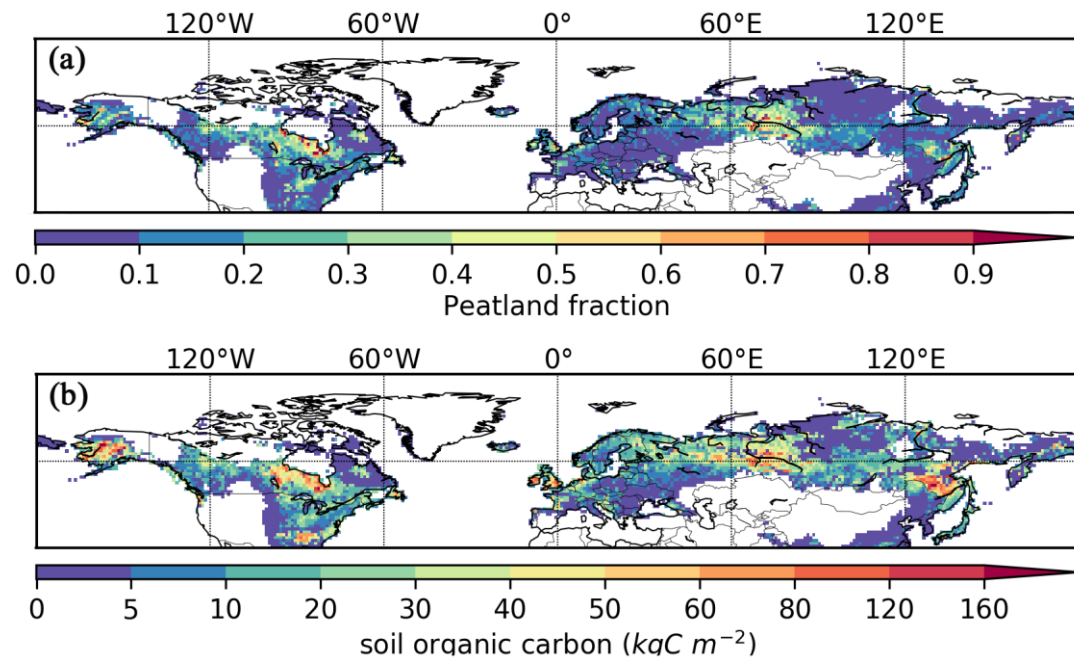
Fig. S12. Simulated peatland area fraction (a) and peat soil carbon density (b) when pattern and timing of ice sheets retreat are not considered (the model was run for 12,000 years), Leptosols and agricultural peatlands are included.
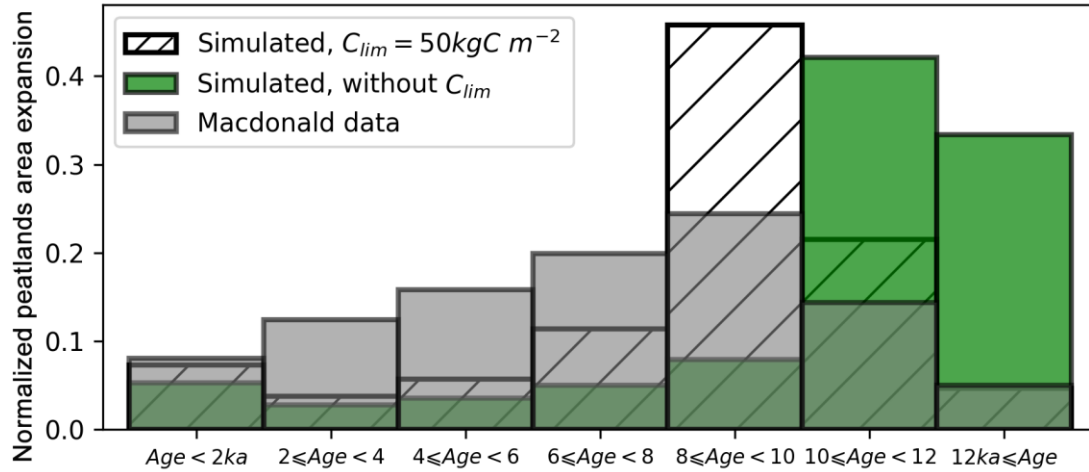
Fig. S13. (Grey bars) Percentage of observed peatland initiation (grey) in 2000-year bins. Peat basal dates of 1516 cores are from MacDonald et al. (2006), peat basal age frequency of each 2000-year bin is divided by the total peat basal age frequency. (White-hatched bars) Percentage of simulated peatlands area developed in each 2000-year bin, deglaciation of ice-sheets is not considered (the model was run for 12,000 years). The peatlands area developed in each bin is divided by the simulated modern (the year 2009) peatlands area. (Green bars) Percentage of simulated peatlands area developed in each 2000-year bin when carbon density criteria (C_{lim}) for peatland expansion has been removed.
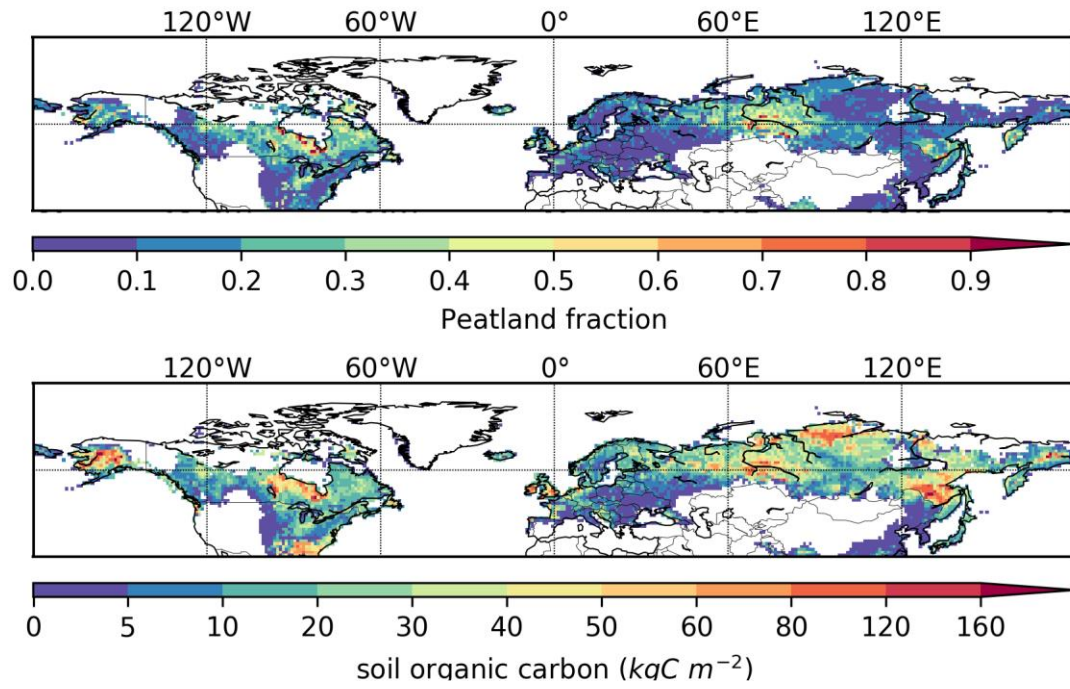
Fig. S14. Same to Fig. S12, but carbon density criteria (C_{lim}) for peatland expansion has been removed.
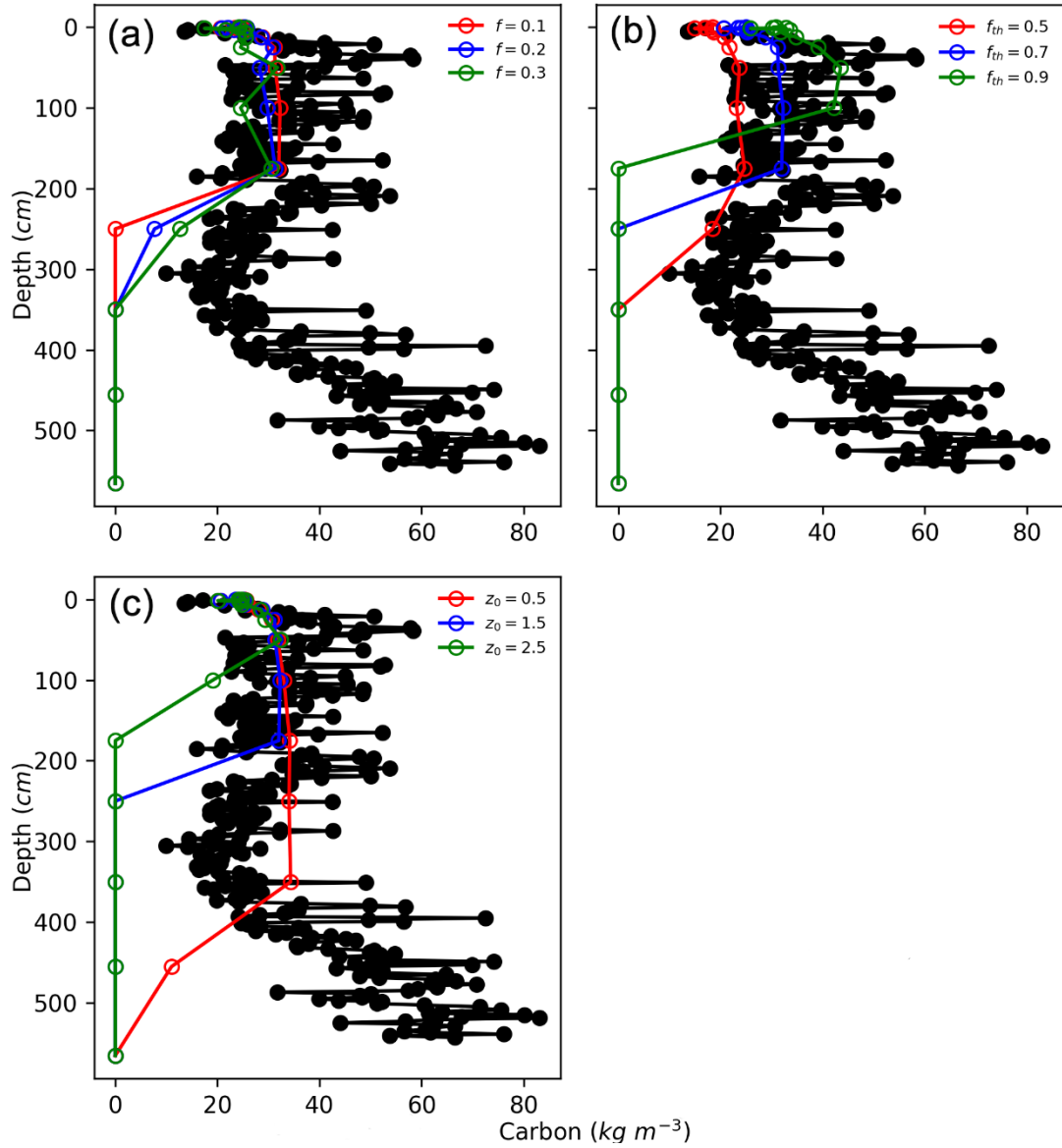
Fig. S15. Observed (black) and simulated (colored) vertical profiles of soil C of Burnt Village. (a) changing the prescribed fraction of C to be transferred (f), (b) changing the prescribed threshold to allow C transfer between soil layers (f_{th}), (c) changing the e-folding depth of intrinsic decomposition rate (z_0, in m).
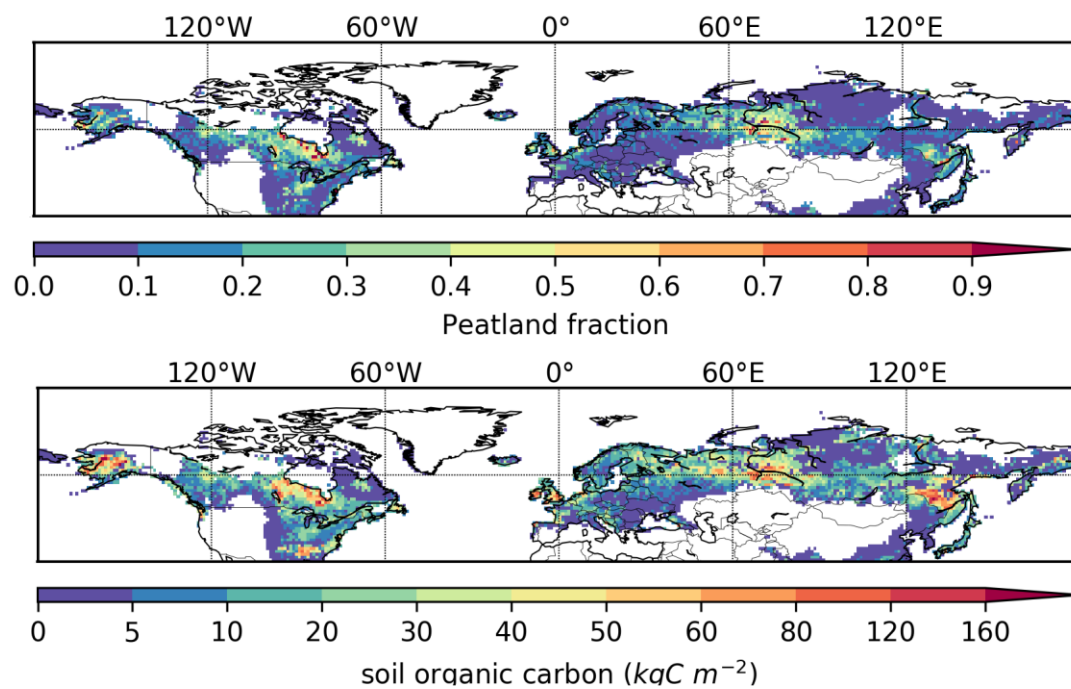
Fig. S16. Same to Fig. S12, but with the prescribed threshold to start C transfer between soil layers $f_{th} = 0.9$.
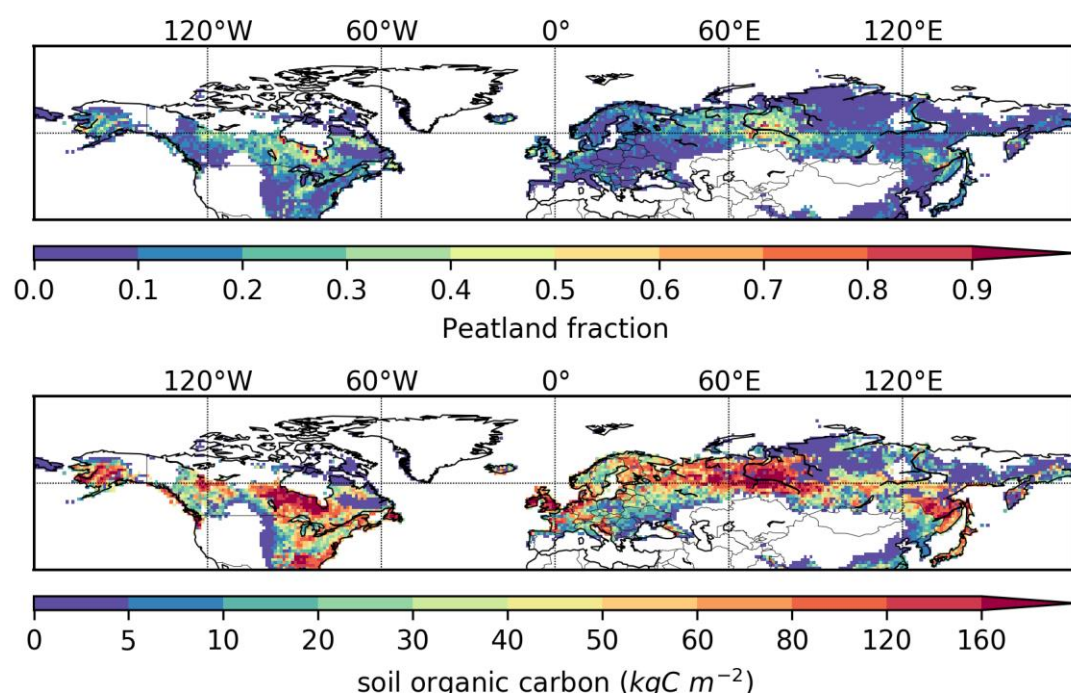
Fig. S17. Same to Fig. S12, but with the e-folding depth of intrinsic decomposition rate $z_0 = 0.5\,m$.
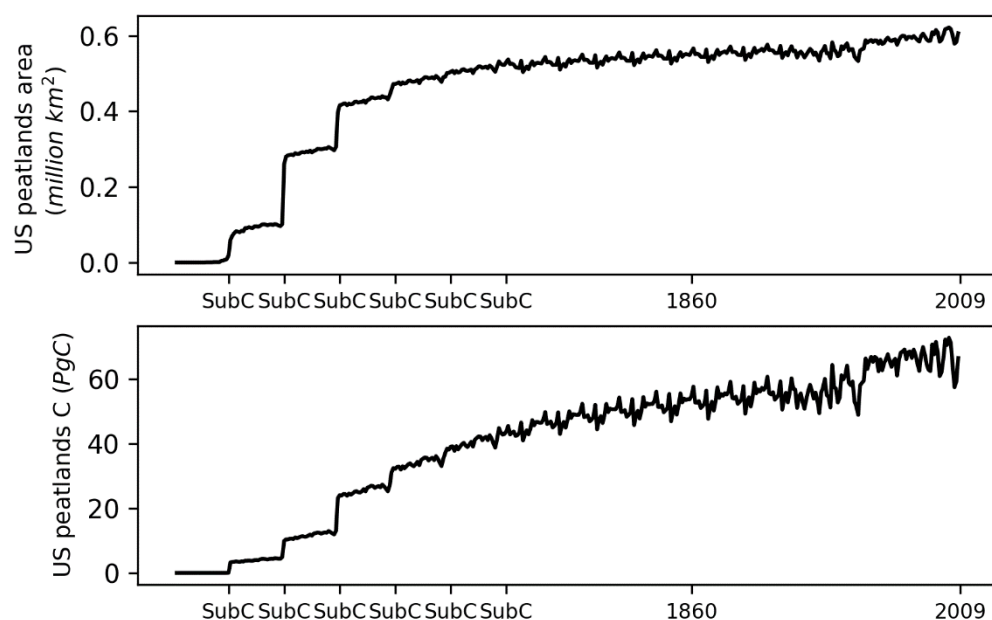
Fig. S18. Simulated peatlands area (upper) and peat soil carbon stock (lower) at the southeastern US.

References

Baird, A. J. and Waldron, S.: Shallow horizontal groundwater flow in peatlands is reduced by bacteriogenic gas production, Geophys. Res. Lett., 30(20), 2003.

Batjes, N. H.: ISRIC-WISE Harmonized Global Soil Profile Dataset (ver.3.1), Rep. 2008/02, (December), 2008.

Batjes, N. H.: Harmonized soil profile data for applications at global and continental scales: Updates to the WISE database, Soil Use Manag., 25(2), 124–127, doi:10.1111/j.1475-2743.2009.00202.x, 2009.

Batjes, N. H.: Harmonized soil property values for broad-scale modelling (WISE30sec) with estimates of global soil carbon stocks, Geoderma, 269(February), 61–68, doi:10.1016/j.geoderma.2016.01.034, 2016.

Boutin, C. and Keddy, P. A.: A Functional Classification of Wetland Plants, J. Veg. Sci., 4(5), 591–600, doi:10.2307/3236124, 1993.

Comas, X., Slater, L. and Reeve, A. S.: Atmospheric pressure drives changes in the vertical distribution of biogenic free-phase gas in a northern peatland, J. Geophys. Res. Biogeosciences, 116(4), doi:10.1029/2011JG001701, 2011.

Donald O. Rosenberry, H.Glaser, P. and Siegel, D. I.: The hydrology of northern peatlands as affected by biogenic gas: current developments and research needs, Hydrol. Process., 20, 3601–3610, doi:10.1002/hyp, 2006.

Dyke, A. S.: An outline of North American deglaciation with emphasis on central and northern Canada, Dev. Quat. Sci., 2(PART B), 373–424, doi:10.1016/S1571-0866(04)80209-4, 2004.

Van Genuchten, M. T.: A closed-form equation for predicting the hydraulic conductivity of unsaturated soils, Soil Sci. Soc. Am. J., 44(5), 892–898, 1980.

Glaser, P. H., Chanton, J. P., Morin, P., Rosenberry, D. O., Siegel, D. I., Ruud, O., Chasar, L. I. and Reeve, A. S.: Surface deformations as indicators of deep ebullition fluxes in a large northern peatland, Global Biogeochem. Cycles, 18(1), doi:10.1029/2003GB002069, 2004.

Gorham, E., Lehman, C., Dyke, A., Janssens, J. and Dyke, L.: Temporal and spatial aspects of peatland initiation following deglaciation in North America, Quat. Sci. Rev., 26(3–4), 300–311, doi:10.1016/j.quascirev.2006.08.008, 2007.

Harden, J. W., Mark, R. K., Sundquist, E. T. and Stallard, R. F.: Dynamics of soil carbon during deglaciation of the laurentide ice sheet., Sci. (New York, NY), 258(5090), 1921–1924, 1992.

Hughes, A. L. C., Gyllencreutz, R., Lohne, Ø. S., Mangerud, J. and Svendsen, J. I.: The last Eurasian ice sheets - a chronological database and time-slice reconstruction, DATED-1, Boreas, 45(1), 1–45, doi:10.1111/bor.12142, 2016.

Joosten, H.: The Global Peatland CO2 picture. Peatland status and drainage related emissions in all countries of the world, Wetl. Int. Ede, 2010 [online] Available from: http://scholar.google.com/scholar?hl=en&btnG=Search&q=intitle:The+Global+Peatland+CO+2+Picture+Peatland+status+and+drainage+related+emissions+in+all+countries+of+the+world#0, 2010.

Kellner, E., Waddington, J. M. and Price, J. S.: Dynamics of biogenic gas bubbles in peat: Potential effects on water storage and peat deformation, Water Resour. Res.,

41(8), 1–12, doi:10.1029/2004WR003732, 2005.

Krinner, G., Viovy, N., de Noblet-Ducoudré, N., Ogée, J., Polcher, J., Friedlingstein, P., Ciais, P., Sitch, S. and Prentice, I. C.: A dynamic global vegetation model for studies of the coupled atmosphere-biosphere system, Global Biogeochem. Cycles, 19(1), 1–33, doi:10.1029/2003GB002199, 2005.

Largeron, C., Krinner, G., Ciais, P. and Brutel-Vuilmet, C.: Implementing northern peatlands in a global land surface model: description and evaluation in the ORCHIDEE high-latitude version model (ORC-HL-PEAT), Geosci. Model Dev., 11(8), 3279–3297, 2018.

Loisel, J., Yu, Z., Beilman, D. W., Camill, P., Alm, J., Amesbury, M. J., Anderson, D., Andersson, S., Bochicchio, C., Barber, K., Belyea, L. R., Bunbury, J., Chambers, F. M., Charman, D. J., De Vleeschouwer, F., Fia kiewicz-Kozie , B., Finkelstein, S. a., Ga ka, M., Garneau, M., Hammarlund, D., Hinchcliffe, W., Holmquist, J., Hughes, P., Jones, M. C., Klein, E. S., Kokfelt, U., Korhola, a., Kuhry, P., Lamarre, a., Lamentowicz, M., Large, D., Lavoie, M., MacDonald, G., Magnan, G., Makila, M., Mallon, G., Mathijssen, P., Mauquoy, D., McCarroll, J., Moore, T. R., Nichols, J., O'Reilly, B., Oksanen, P., Packalen, M., Peteet, D., Richard, P. J., Robinson, S., Ronkainen, T., Rundgren, M., Sannel, a. B. K., Tarnocai, C., Thom, T., Tuittila, E.-S., Turetsky, M., Valiranta, M., van der Linden, M., van Geel, B., van Bellen, S., Vitt, D., Zhao, Y. and Zhou, W.: A database and synthesis of northern peatland soil properties and Holocene carbon and nitrogen accumulation, The Holocene, 24(9), 1028–1042, doi:10.1177/0959683614538073, 2014.

MacDonald, G. M., Beilman, D. W., Kremenetski, K. V., Sheng, Y., Smith, L. C. and Velichko, A. A.: Rapid Early Development of Circumarctic Peatlands and Atmospheric CH4 and CO2 Variations, Science (80-.)., 314(5797), 285–288, doi:10.1126/science.1131722, 2006.

Moyano, F. E., Vasilyeva, N., Bouckaert, L., Cook, F., Craine, J., Curiel Yuste, J., Don, A., Epron, D., Formanek, P., Franzluebbers, A., Ilstedt, U., Kätterer, T., Orchard, V., Reichstein, M., Rey, A., Ruamps, L., Subke, J. A., Thomsen, I. K. and Chenu, C.: The moisture response of soil heterotrophic respiration: Interaction with soil properties, Biogeosciences, 9(3), 1173–1182, doi:10.5194/bg-9-1173-2012, 2012.

Mualem, Y.: A new model for predicting the hydraulic conductivity of unsaturated porous media, Water Resour. Res., 12(3), 513–522, 1976.

Parton, W. J., Stewart, J. W. B. and Cole, C. V: Dynamics of C , N , P and S in grassland soils : a model, Biogeochemistry, 131(5), 109–131, 1988.

Payette, S.: Peat inception and climatic change in northern Quebec, in Climatic Changes on a Yearly to Millennial Basis, pp. 173–179, Springer., 1984.

Qiu, C., Zhu, D., Ciais, P., Guenet, B., Krinner, G., Peng, S., Aurela, M., Bernhofer, C., Brümmer, C., Bret-Harte, S., Chu, H., Chen, J., Desai, A. R., Dušek, J., Euskirchen, E. S., Fortuniak, K., Flanagan, L. B., Friborg, T., Grygoruk, M., Gogo, S., Grünwald, T., Hansen, B. U., Holl, D., Humphreys, E., Hurkuck, M., Kiely, G., Klatt, J., Kutzbach, L., Largeron, C., Laggoun-Défarge, F., Lund, M., Lafleur, P. M., Li, X., Mammarella, I., Merbold, L., Nilsson, M. B., Olejnik, J., Ottosson-Löfvenius, M., Oechel, W., Parmentier, F.-J. W., Peichl, M., Pirk, N., Peltola, O., Pawlak, W.,

Rasse, D., Rinne, J., Shaver, G., Schmid, H. P., Sottocornola, M., Steinbrecher, R., Sachs, T., Urbaniak, M., Zona, D. and Ziemblinska, K.: ORCHIDEE-PEAT (revision 4596), a model for northern peatland CO2, water, and energy fluxes on daily to annual scales, Geosci. Model Dev., 11(2), 497–519, doi:10.5194/gmd-11-497-2018, 2018.

Romanowicz, E. A., Chanton, J. P. and Glaser, P. H.: Temporal variations in dissolved methane deep in the Lake Agassiz Peatlands, Minnesota, Global Biogeochem. Cycles, 9(2), 197–212, 1995.

De Rosnay, P., Bruen, M. and Polcher, J.: Sensitivity of surface fluxes to the number of layers in the soil model used in GCMs, Geophys. Res. Lett., 27(20), 3329–3332, 2000.

De Rosnay, P., Polcher, J., Bruen, M. and Laval, K.: Impact of a physically based soil water flow and soil-plant interaction representation for modeling large-scale land surface processes, J. Geophys. Res. Atmos., 107(D11), 2002.

Stocker, B. D., Spahni, R. and Joos, F.: DYPTOP: A cost-efficient TOPMODEL implementation to simulate sub-grid spatio-temporal dynamics of global wetlands and peatlands, Geosci. Model Dev., 7(6), 3089–3110, doi:10.5194/gmd-7-3089-2014, 2014.

Strack, M., Kellner, E. and Waddington, J. M.: Dynamics of biogenic gas bubbles in peat and their effects on peatland biogeochemistry, Global Biogeochem. Cycles, 19(1), 1–9, doi:10.1029/2004GB002330, 2005.

Strack, M., Kellner, E. and Waddington, J. M.: Effect of entrapped gas on peatland surface level fluctuations, Hydrol. Process., 20(17), 3611–3622, doi:10.1002/hyp, 2006.

Tootchi, A., Jost, A. and Ducharne, A.: Multi-source global wetland maps combining surface water imagery and groundwater constraints, Earth Syst. Sci. Data Discuss., 2018, 1–44, doi:10.5194/essd-2018-87, 2018.

Zhu, D., Peng, S., Ciais, P., Zech, R., Krinner, G., Zimov, S. and Grosse, G.: Simulating soil organic carbon in yedoma deposits during the Last Glacial Maximum in a land surface model, Geophys. Res. Lett., 43(10), 5133–5142, doi:10.1002/2016GL068874, 2016.